

# Findings of sub- $T_g$ endotherm in vapor-deposited ultrastable phenolphthalein glass

Soichi Tatsumi,<sup>\*</sup> Yutaka Nakamura, Takashi Miyazaki, Tomohiro Kayano , Daiki  
Kishimoto , Susumu Fujiwara, and Haruhiko Yao

*Kyoto Institute of Technology, Hashiue-cho, Matsugasaki, Sakyo-ku, Kyoto, 606-8585,  
Japan*

E-mail: statsumi@kit.ac.jp

## Abstract

We have performed differential scanning calorimetric and synchrotron x-ray diffraction studies to elucidate the nature of vapor-deposited ultrastable phenolphthalein glass. As a result, we found that phenolphthalein forms the ultrastable glass by depositing at 313 K, which is about 0.86 times the ordinal glass transition temperature of 361 K. As previous ultrastable glass studies reported, this ultrastable state involved an anisotropic structure. In addition, we found that a large endotherm (sub- $T_g$  endotherm) was observed in the temperature range between deposition and ordinal glass transition temperatures. We have assessed the stability of deposited states thermodynamically and found that those states are much more stable than those crystalline states when the deposition rate is small enough. The total enthalpies associated with the sub- $T_g$  endotherm are roughly proportional to the powers of the inversed thickness of the deposited glass. Despite the thermodynamical evidence, wide-angle x-ray diffraction of the structure associated with the sub- $T_g$  endotherm was unchanged. Following our findings, we have proposed a scenario in which ultrastable vapor-deposited phenolphthalein glass is rooted in locally superstable structure. Our locally oriented scenario would be universal for forming stable structures in other vapor-deposited glasses.

## 1. Introduction

When liquid is quenched without crystallization, its molecules become immobile while sustaining an amorphous structure at a specific temperature, the *glass transition temperature*,  $T_g$ . This phenomenon is known to be universal throughout various systems.<sup>1</sup> Thankfulness to this universality, the application of this glassy state is varied: the new memory device with the warranty of lengthy time stability,<sup>2,3</sup> the drug production process to achieve good absorbance to the human body,<sup>4,5</sup> the understanding of cryoprotection in biological systems, which sometimes referred as cryptobiosis,<sup>6-8</sup> etc. To enrich and fulfill our daily life, it is important to understand the glassy state and the mechanism to reach it.

Since the glassy state is a non-equilibrium state owing to its definition, the physical properties of the resulting state strongly depend on the thermal history.<sup>9-11</sup> In particular, it is well known that the enthalpy or specific volume represents stability. A stable glass, with a low enthalpic state, is often achieved by cooling as slowly as possible or annealing at an appropriate temperature for a long time. As an extreme example, the amber resin, which was vitrified tens of millions to 100 million years ago, was reported to change into a stable glass over a lengthy time.<sup>12,13</sup>

The physical vapor deposition (PVD) method has recently drawn much attention to constructing a stable glass to bypass the enormous amount of time.<sup>1,14,15</sup> According to the PVD method, gaseous molecules are attached to the substrate at a sustaining low temperature to ensure a great drop in the energy of molecules to prevent crystallization. The rate of quenching in the PVD method is the fastest compared to the experimentally achievable ones. With a straight deductive consequence, the outcome of the realized amorphous state is plausible to have very high enthalpy with reflection of the randomness of gaseous molecules. When the deposition temperature of the substrate,  $T_d$ , is considerably low,<sup>16,17</sup> this deduction meets well, however, when  $T_d$  is controlled with just below  $T_g$  of the molecules, in precise,  $T_d/T_g \simeq 0.8 \sim 0.9$ , the outcome of the realized amorphous state is known to have significantly low enthalpic state, which is so-called the *ultrastable glass*.<sup>14,18-20</sup> Under the assumption that the vapor-deposited (VD) glass was the extrapolated state from liquid-quenched (LQ) glass, the enthalpic analysis tells the equivalency between ultrastable VD glass and LQ glass annealed for billions of years.<sup>1,15,21</sup>

We look into the differences between ultrastable VD glass and LQ glass. In particular, we would like to focus on two phenomena. The former is the appearance of the medium ranged order (MRO), typically with the size of 2-3 constituent molecules,<sup>22-24</sup> and the latter is the absence of the low-temperature heat capacity proportional to absolute temperature. For the former, the MRO appeared as the anisotropic structure and was given the statements as an enhancement to the molecular anisotropy during the deposition process. However, as

carbon tetrachloride demonstrates the ultrastable VD glass,<sup>25</sup> the asymmetry of molecules is not a necessary condition. For the latter, while the LQ glass shows the low-temperature heat capacity proportional to absolute temperature, the ultrastable VD glass does not show any relevant features. Since a long-aged amber glass demonstrates low-temperature heat capacity, this feature should not root in the stability. Considering the low-temperature heat capacity, the ultrastable VD glass is more like a crystalline state. Consequently, we shall say the assumption of the equivalency between LQ and VD glass is not firm to stand on.

We aim to deepen our knowledge about the nature of ultrastable glass by bringing a new perspective. In the study of ultrastable VD glass, we usually focus on thermal properties at temperatures higher than the ordinal  $T_g$ , rooting to the presence of the remarkably large endotherm accompanied by the devitrification process, however, we also spotlight thermal properties at temperatures lower than ordinal  $T_g$  in this article. As a result, we have found a thermal anomaly in this region as an endothermic effect, which we call *sub- $T_g$  endotherm*. This kind of anomaly has not been well focused on before, but similar results are shown in the previous studies by Yu et al. for metallic glass. They showed the existence of sub- $T_g$  endotherm for the vapor-deposited  $\text{Zr}_{65}\text{Cu}_{27.5}\text{Al}_{7.5}$ <sup>26–28</sup> and discussed the relation with the secondary relaxation.

This paper concerns the thermal properties and structural variance for ultrastable VD phenolphthalein. Firstly, we introduce our experimental setup for DSC and x-ray diffraction study in Sec.2. Among them, in-house high-sensitive DSC is particularly important. Then, we describe the devitrification behavior of an as-deposited sample and an annealed sample of ultrastable VD phenolphthalein glass, along with details of the behavior of sub- $T_g$  endotherm in Sec.3.1. After all, we discuss those fictive temperatures in Sec.3.2. Then, we examine the structural changes in ultrastable vapor-deposited phenolphthalein glass based on the results of powder X-ray diffraction in Sec.3.3. Next, we analyze the thermal properties of sub- $T_g$  endotherm with a focus on sample thickness dependence by using high-sensitive DSC in Sec.3.4 to Sec.3.6. Finally, we discuss the origin of super-stabilities in VD phenolphthalein

glass and propose the scenario to explain ultrastable VD phenolphthalein glass rooting to the locally superstable structure.

## 2. Experimental

### 2.1. Sample preparation

Reagent grade phenolphthalein(purity of 98 wt.%, melting temperature  $T_m = 533$  K) and acetone were purchased from Wako Pure Chemical Corp. and used without further purification. Phenolphthalein acetone solution was dried on a dish-like copper plate served as a deposition source to obtain a flat and smooth surface of solid phenolphthalein.

The schematic view of a PVD apparatus is shown in Fig. 1. The chamber was evacuated under 2-3 mPa using a diffusion pump system (SINKU KIKO Inc., VPC-050). The deposition source was fixed on a temperature-controlled copper heater block. Substrates, i.e. a polyimide(PI) film (DuPont-Toray Co. Ltd., Kapton 20 EN, 50 mm x 50 mm x 5  $\mu$ m) for calorimetry and silicon wafers (Canosis Co., Ltd., 10 mm x 10 mm x 0.28 mm) for x-ray diffraction, were attached to the temperature-controlled aluminum plate that had a quartz crystal microbalance (QCM) (ULVAC Inc., UCR-5MAU-12) at its center for measuring deposition thickness,  $d_{\text{QCM}}$ . The time evolution of  $d_{\text{QCM}}$  was measured with a deposition controller (ULVAC Inc., CRTM-6000G). The temperature dependence and deposition thickness histogram of  $v_d$  are shown in Figs. 1(b) and (c), respectively. Since phenolphthalein is a sublimation substance,  $v_d$  depends on not only the temperature but also the surface area(roughness) of a deposition source. Therefore, the surface of solid phenolphthalein was made to be flat and smooth to control  $v_d$  with the temperature of the source,  $T_s$ .

Deposited samples having different  $d_{\text{QCM}}$  were measured with a thermogravimetric analyzer (TG) (TA Instruments, Discovery TGA) upon a heating scan and their deposited masses,  $m_{\text{TG}}$ , were determined from mass losses due to the evaporation of phenolphthalein and the results were shown in Fig.1(d).  $m_{\text{TG}}$  was proportional to  $d_{\text{QCM}}$  as shown in Fig. 1(d).

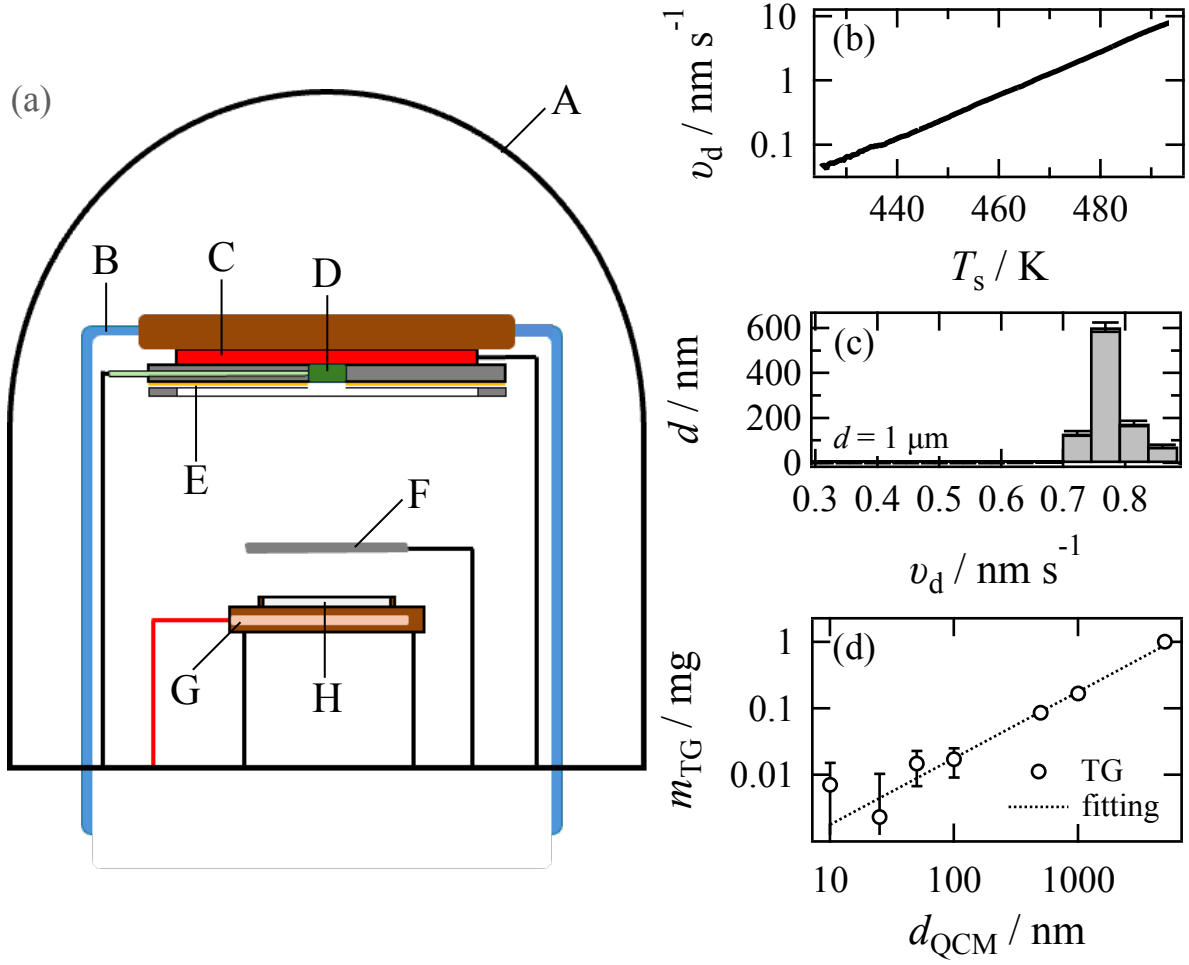


Figure 1: (a) The schematic view of a physical vapor deposition apparatus. A: Vacuum chamber. B: Coolant. C: Peltier modules. D: Quartz crystal microbalance. E: Deposition surface. F: Shutter. G: Heater block. H: Deposition source. (b) The dependence of deposition rate,  $v_d$ , on the temperature of the deposition source,  $T_s$ . (c) The histogram of  $v_d$ . (d) Deposition thickness  $d_{\text{QCM}}$  measured with a quartz crystal microbalance vs. deposited mass  $m_{\text{TG}}$  determined with a thermogravimetric analyzer.

Using the linear relationship,  $d_{\text{QCM}}$  values were calibrated assuming that the densities of the crystalline and glassy states are the same. Calibrated deposition thickness,  $d$ , were ranging from 5 nm to 10  $\mu\text{m}$ . The deposition rate,  $v_d$ , was derived from the numerical differentiation of  $d$  with respect to time.

## 2.2. Differential scanning calorimetry

Phenolphthalein deposited PI films were punched out with a precise circular hand punch (Nogamigiken Co. Ltd.,  $\phi 5.00$  mm), and the fifteen punch-out films were put in an aluminum crimp pan (Shimadzu Corp., S201-52943).

The thermograms of samples with  $d \geq 5 \mu\text{m}$  ( $m_{\text{TG}} \geq 1.8$  mg) were measured with a conventional differential scanning calorimeter (DSC) (TA Instruments Inc., DSC2920). It allowed the determination of heat capacity over a wide range as well as the enthalpy of fusion to evaluate the excess enthalpy of the liquid and glassy states and the fictive temperature of the glass transition,  $T_f$ . Typical temperature profile is shown in Fig. 2(b).

The thermograms of samples with  $d < 5 \mu\text{m}$  ( $m_{\text{TG}} < 1.8$  mg) were measured with a high-sensitivity differential scanning calorimeter (HSDSC) at a scanning rate of 1 K/min in the range from 268 K to 408 K. Typical temperature profile is shown in Fig. 2(c).

The details of HSDSC will be reported elsewhere,<sup>29</sup> we describe it briefly. The schematics of HSDSC are shown in Fig. 2(a). Heat flux difference between sample and reference cells was measured using two thermoelectric modules (Ferrotec Corp., 9500/018/012) consisting of eighteen pairs of  $\text{Bi}_2\text{-Te}_3$  thermoelectric elements. As a result, HSDSC has a high sensitivity of  $\pm 2$  nW, which enables measurements for an ultra-thin sample with  $d = 5$  nm ( $m_{\text{TG}} < 1.8 \mu\text{g}$ ). A high sensitivity of  $\pm 5$  nW was achieved using two miniature thermoelectric modules in the nano-watt stabilized DSC.<sup>30</sup> However, owing to the two-stage thermal RC high-cut filter for dumping temperature fluctuation of sample and reference cells, the temperature scanning rate was limited up to 0.06 K/min. The same dumping effect was realized with a single-stage thermal RC high-cut filter using silicone rubber foam as a thermal resistance,

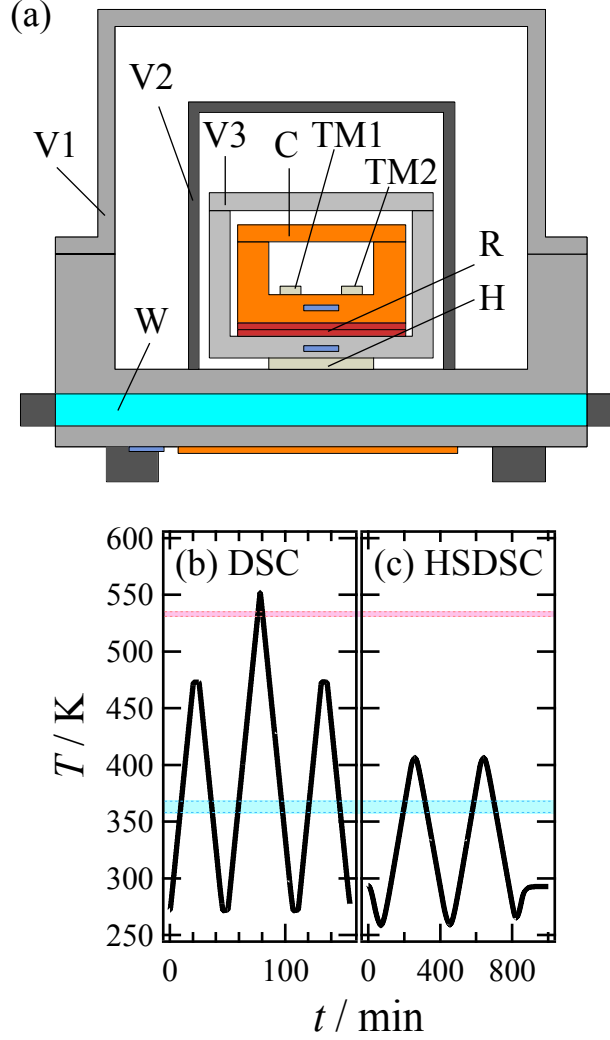


Figure 2: (a) Schematic view of high-sensitivity differential scanning calorimeter (HSDSC). V1-V3: Aluminum shields. TM1, TM2: Thermoelectric modules. C: Copper block. R: Silicone rubber foam. H: Peltier module. W: Cooling water. (b) Temperature profile of a DSC measurement. (c) Temperature profile of an HSDSC measurement. Upper and lower horizontal lines indicate the melting and glass transition temperatures of phenolphthalein, respectively.

maximum temperature scanning rate was improved to 1 K/min in HSDSC.

### 2.3. X-ray diffraction

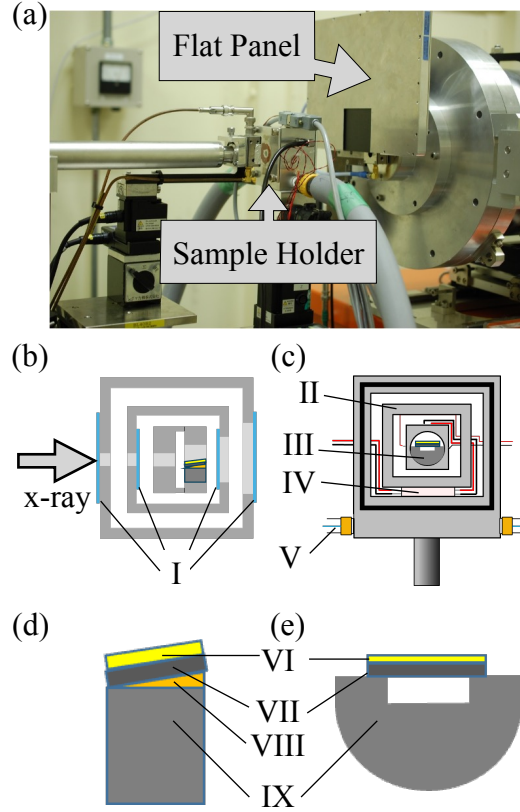


Figure 3: (a) Photograph of the sample holder in the BL40B2 beamline. (b) Side view and (c) front view of a temperature-controlled sample holder. (d) side view and (e) front view of a sample stage. I: Amorphous PEEK films. II: Aluminum heat bath. III: Sample stage. IV: Peltier module. V: Cooling water. VI: Deposited phenolphthalein film. VII: Silicon wafer. VIII: Thermal conductive adhesive tape. IX: Aluminum sample stage.

(100) oriented silicon wafers were used as deposition substrates to avoid diffraction from silicon. We have confirmed that the thermograms of phenolphthalein on PI film and silicon wafer were the same (data not shown).

X-ray diffraction measurements were performed at the BL40B2 beamline in SPring-8 (Hyogo, Japan). Wide-angle x-ray diffraction (WAXD) images of deposited phenolphthalein films were measured using a flat panel sensor (Hamamatsu Photonics K.K., C9728DK-10) with a wavelength of 0.10 nm and a camera length of 105 mm in reflection geometry. The

temperature of a sample was scanned from 270 K to 400 K at 2 K/min with a sample holder shown in Fig. 3, which temperature was controlled within  $\pm 0.1$  K using a programmable temperature controller (Shimaden Co. Ltd., SR23). The temperature dependence of WAXD images was taken every 15 s with an exposure time of 14 s.

## 3. Results

### 3.1. Sub- $T_g$ endotherm

In this section, we demonstrate the appearance of the sub- $T_g$  endotherm in VD phenolphthalein glass and introduce its thermal properties based on the conventional DSC results. Figure 4 represents DSC results obtained by two different thermal profiles for identical samples deposited at  $T_d=313$  K and  $v_d= 2.67$  nm/s with  $d \approx 10$   $\mu\text{m}$ . Figure 4(a) represents Sample A to show the property of as-deposited phenolphthalein glass and the appearance of the sub- $T_g$  endotherm. Figure 4(b) represents Sample B to show the irreversibilities of the sub- $T_g$  endotherm with the annealing effect. In both figures, the upper parts represent the temperature profiles between 268 K and 513 K at a scanning rate of 10 K/min, and the lower parts represent corresponding heat capacities for heating scans.

As is shown in Fig. 4, VD phenolphthalein exhibits thermal anomaly indicated with numbers. **1** indicates a characteristic endotherm denoted as sub- $T_g$  endotherm around the temperature from 290 K to 360 K. **2** indicates a devitrification temperature,  $T_{\text{dev}}$ , which involves a large endotherm at around 380 K. **3** indicates crystallization temperature,  $T_c$ , at around 410 K. **4** indicates melting temperature,  $T_m = 533$  K. Finally, **5** indicates ordinal glass transition temperature,  $T_g = 361$  K. While the sub- $T_g$  endotherm has not been reported in organic VD glass before, a large endotherm involved with devitrification and the following exotherm involved with crystallization is frequently seen in ultrastable VD glass.

From the comparison between Sample A and Sample B, the sub- $T_g$  endotherm has irreversibilities with the thermal treatment. The dotted green line in the upper panel of Fig. 4(b)

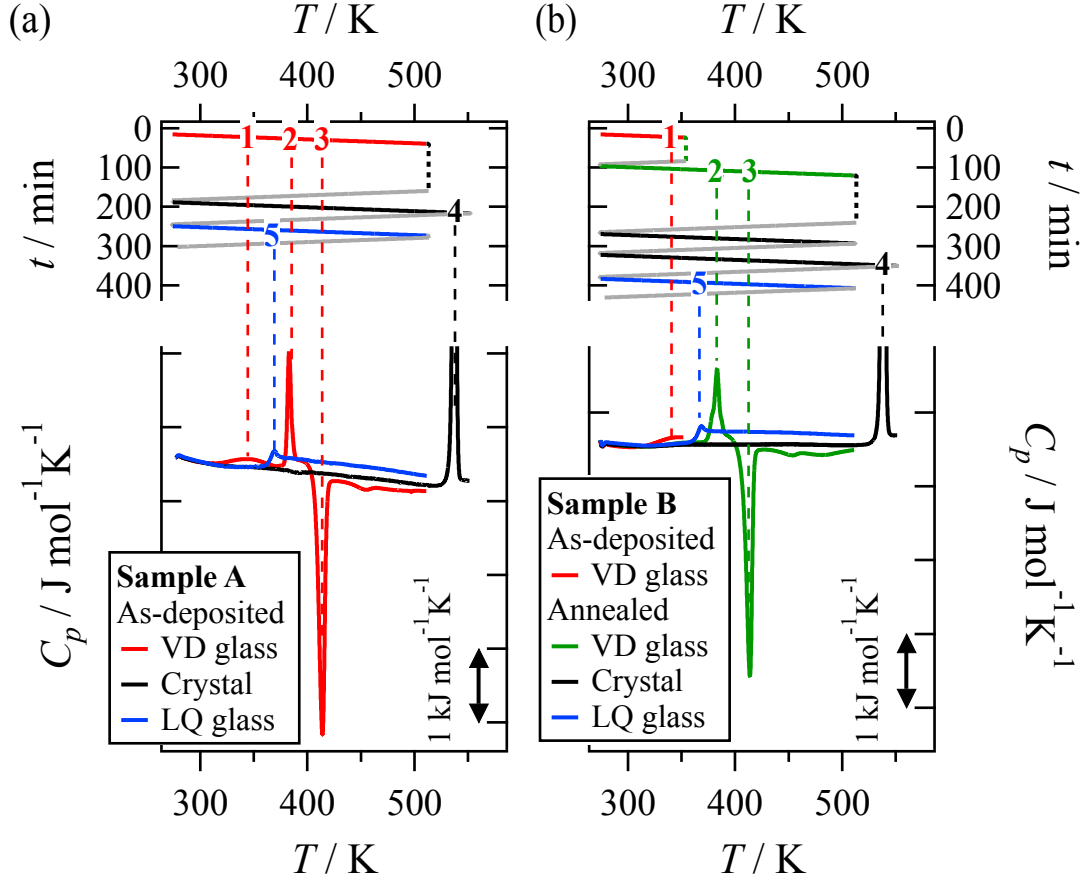


Figure 4: Heat capacities of VD phenolphthalein glass for (a) Sample A and (b) Sample B. The upper and the lower panel indicate the temperature profile and heat capacity, respectively. Numbers in both figures indicate **1**; sub- $T_g$  endotherm, **2**; devitrification, **3**; crystallization, **4**; melting, and **5**; ordinal glass transition. In both figures, red, black, and blue lines correspond to the as-deposited, crystalline, and liquid-quenched states. The black dotted line indicates the annealing procedure to make the sample crystallize completely. The green dotted line in (b) indicates the annealing procedure to erase the sub- $T_g$  endotherm and subsequently, the green line corresponds to the annealed state. The deposition temperature  $T_d$ , deposition rate  $v_d$ , and thickness  $d$  of sample are 313 K, 2.67 nm/s, and ca. 10  $\mu\text{m}$ , respectively.

indicates the annealing procedure at around 353K for 1 hour. This process is applied at just below ordinal  $T_g$  and eliminates the sub- $T_g$  endotherm from Sample B. Its heat capacity demonstrates this elimination as the green line in the lower panel of Fig. 4(b) shows.

In all DSC measurements, as is shown in the dotted black line in the upper panel of Fig. 4, samples were annealed at 513K, corresponding to just above crystallization temperature,  $T_c$ , for 2 hours to crystallize the sample completely. The crystallized sample is heated to 553 K to melt the sample. The total endotherm accompanied by melting gives the amounts of samples. Then, the melt is turned to the LQ glass with cooling. Its heat capacity is shown in the blue line in Fig. 4.

### 3.2. Anomalous fictive temperature involved with sub- $T_g$ endotherm

To assess the stability of each state, we calculate a *fictive temperature*,  $T_f$ . The term fictive temperature is widely used in the glass community<sup>15,18,20,31</sup> and corresponds to the temperature an equilibrated material would have. Its behaviors determined by other observables, such as the relaxation time, were to exhibit the same with equilibrated material with indicated  $T_f$ . Practically,  $T_f$  is derived by using the enthalpic diagram by taking the cross-section of the enthalpy of the glassy state and the extrapolation of the enthalpy of the liquid from high temperature to low temperature.

At first, the excess heat capacity,  $\Delta C_p$ , is defined as the difference between the heat capacities of super-cooled liquid  $C_p^{\text{liquid}}$  and those of crystal  $C_p^{\text{crystal}}$ ,

$$\Delta C_p(T) = C_p^{\text{liquid}}(T) - C_p^{\text{crystal}}(T). \quad (1)$$

The temperature dependencies of  $\Delta C_p$  are shown in Fig. 5(a). The red, green, and blue lines represent the excess heat capacity of the as-deposited, annealed, and liquid-quenched states, respectively. As in Fig. 4, the disappearance of sub- $T_g$  endotherm with the annealing procedure is seen. The green dotted line indicates the pre-annealed state which should be

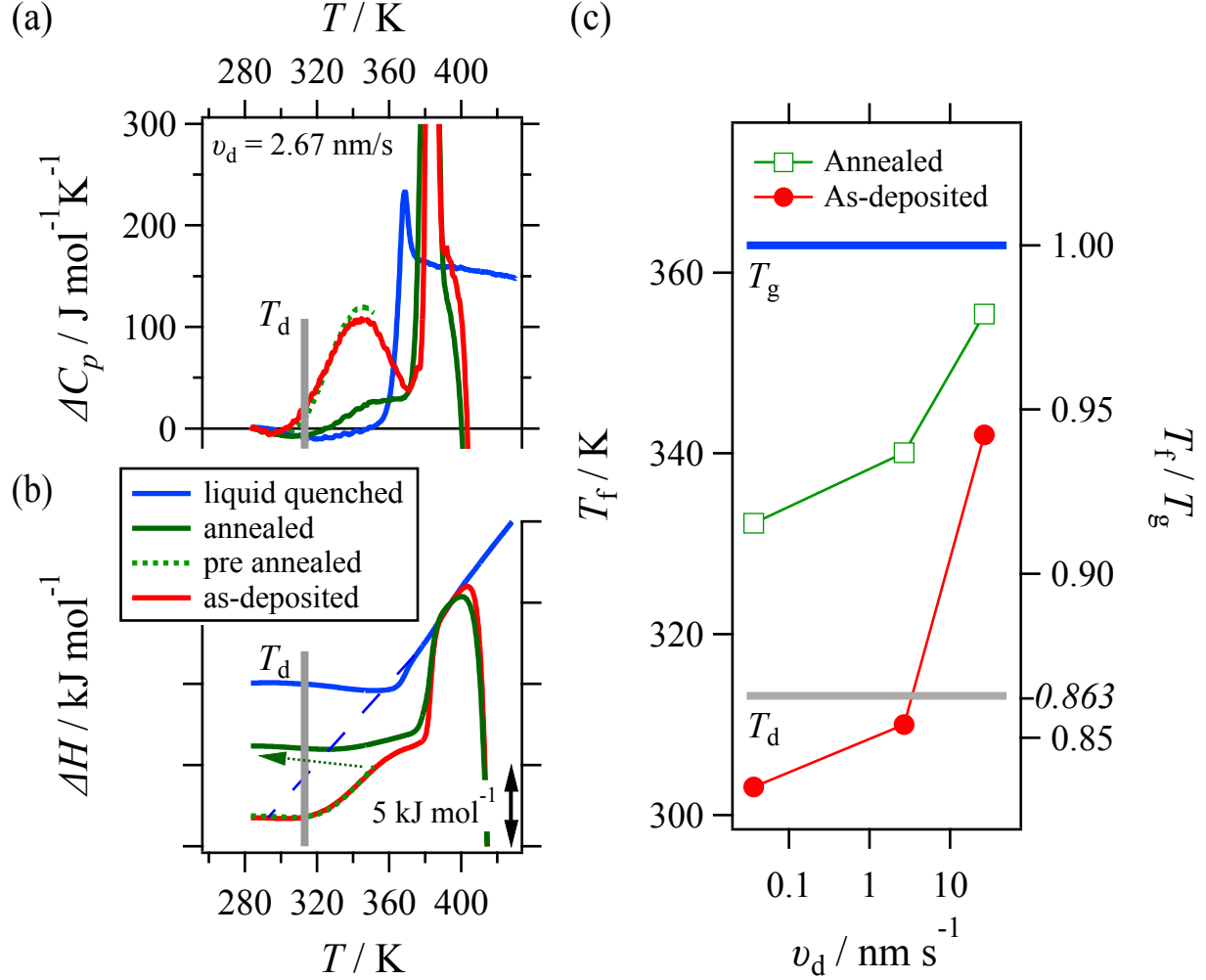


Figure 5: (a) The excess heat capacities and (b) the excess enthalpies as a function of temperatures for liquid quenched (blue line), annealed at 353 K (green line), and as-deposited (red line) glasses with those deposition rates as 2.67 nm/s. The dotted green line indicates those of pre-annealed glass to demonstrate good correspondencies to the as-deposited sample. The broken blue line in (b) indicates the extrapolation of liquid quenched glass to obtain corresponding  $T_f$  in each sample. Obtained  $T_f$  as a function of deposition rate is shown in (c). Blue and gray lines indicate  $T_g$  and  $T_d$ , respectively.

equivalent to the as-deposited state. The sharp drop in excess heat capacities immediately after devitrification reflects the exothermic effect associated with crystallization.

Next, we calculate the excess enthalpy,  $\Delta H(T)$ , which is shown in Fig. 5(b).  $\Delta H(T)$  is the excess enthalpy of liquid and glassy states against the crystalline state. Ideally, this could be calculated by integrating  $\Delta C_p$  as,

$$\Delta H(T) = \Delta_m H - \int_T^{T_m} \Delta C_p(T) dT. \quad (2)$$

Here,  $\Delta_m H$  corresponds to the enthalpy of the fusion. However, since vapor-deposited phenolphthalein glass always exhibits crystallization after a vitrification event, we need to assess the enthalpy of crystallization at the same time. To avoid this difficulty, we stand with the hypothesis that vapor-deposited phenolphthalein glass always falls into the liquid state after devitrification. At around 380 K, just after devitrification, all the state has identical enthalpic values as is shown in Fig. 5(b). Then,  $\Delta H(T)$  is calculated as

$$\Delta H(T) = \int_{T=380 \text{ K}}^T \Delta C_p(T) dT + \Delta H^0. \quad (3)$$

$\Delta H^0$  is a constant related to the arbitrariness of enthalpy and is common in every state.

Finally, by consulting the enthalpy diagram shown in Fig. 5,  $T_f$  is elucidated. As Fig. 5(c) demonstrates  $v_d$  dependencies of  $T_f$ , in both as-deposited and annealed glasses, the lower the  $v_d$  is, the smaller the  $T_f$  is. This  $v_d$  dependence is consistent with previous studies.<sup>18</sup> Edgier's group has investigated the system for Indomethacin and 1,3,5-Tri(1-naphthyl)benzene to show the same dependencies. Generally speaking, the vapor-deposited ultrastable glass was expected to be extrapolated from the liquid-quenched glass, which would make a lengthy annealing time. It means  $T_f$  should be larger than  $T_d$ . However, in some cases, designated  $T_f$  in as-deposited glass is smaller than  $T_d$ , which is the temperature to realize vapor-deposited glass. This odd phenomenon has not yet been reported in many previous studies for  $T_f$  in vapor-deposited glass.

### 3.3. Structural variation accompanied with sub- $T_g$ endotherm

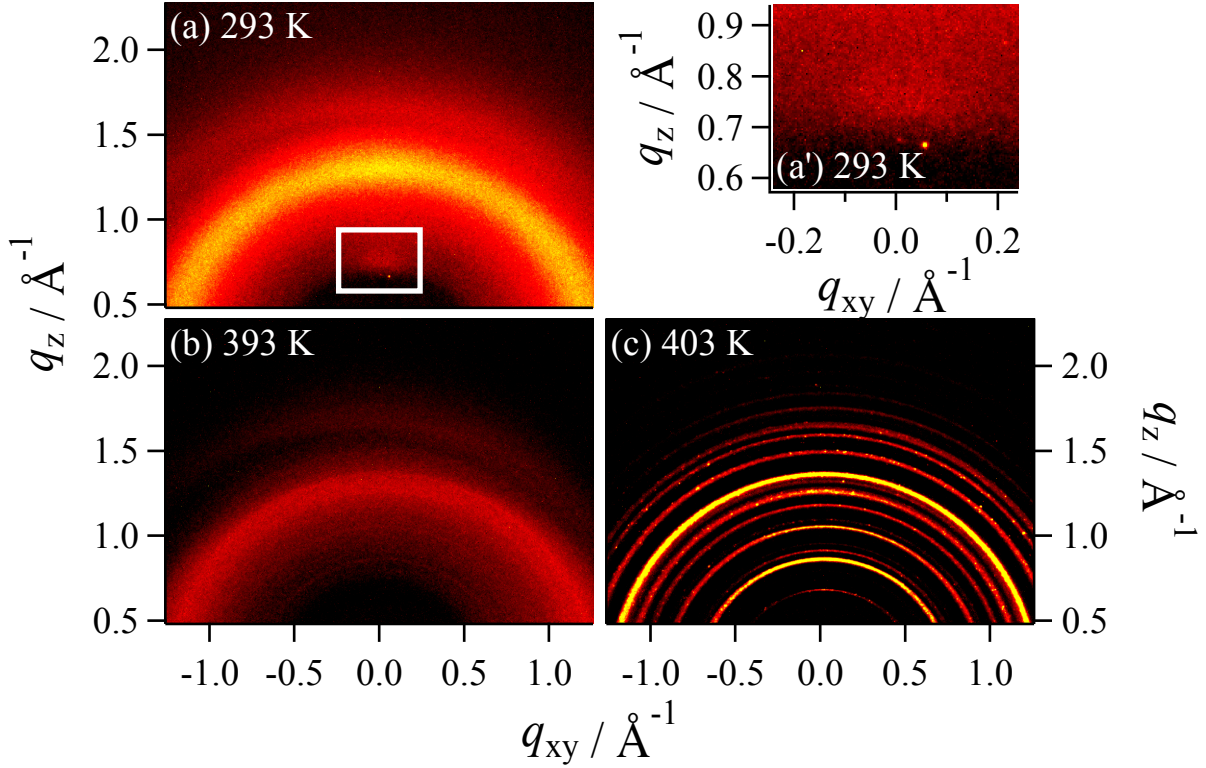


Figure 6: Temperature evolutions of the 2D scattering patterns of the WAXS results for the sample made by vapor-deposition with the  $T_d$  of 313 K. (a) indicates a snapshot at 293 K, which corresponds to the as-deposited state. A blurred semicircular arc, typical in amorphous materials, and a broad bright spot, indicating the emergence of medium-range order (MRO) perpendicular to the deposited surface, are seen. (a') is corresponding to the region which indicates a white rectangle in Fig. (a). A close-up of the broad bright spot is shown. (b) indicates a snapshot at 393 K. The sample is on over-quenched liquid just after experiencing the devitrification event. While the blurred semicircular arc is still alive, the bright spot has disappeared. (c) indicates a snapshot at 403 K. The sample is just after experiencing cold crystallization.

The topic of this section is the structural variance accompanied with sub- $T_g$  endotherm,  $T_{\text{dev}}$ , and  $T_c$ , based on the X-ray powder diffraction patterns of samples obtained at Spring-8 as is shown in Sec.2.3. Samples were deposited with  $T_d = 313$  K and subsequently scanned over the range of 293  $\sim$  403 K with increasing temperature.

Figures 6(a-c) represent the 2D diffraction pattern obtained at 293 K, 393 K, and 403 K,

respectively. Figures 6(a) and 6(b) demonstrate a broad amorphous peak around  $q \sim 1.3 \text{ \AA}^{-1}$  that is equally distributed azimuthally. We attribute this amorphous peak to the distance between the nearest neighboring phenolphthalein molecules in real space ( $\sim 5 \text{ \AA}$ ). On the other hand, only Fig. 6(a) shows a broad spot around  $q \sim 0.7 \text{ \AA}^{-1}$  which indicates the appearance of the stacking structure, where its typical size is about  $10 \text{ \AA}$ , in the direction perpendicular to the deposited surface (shown in the white square in Fig. 6(a)). It means the appearance of the anisotropic medium-range order (AMRO). An enlarged view of AMRO is shown in Fig. 6(a'). As many previous studies discussed,<sup>14,24,31</sup> the formation of AMRO in the ultrastable VD glass is a distinguishable feature against the ordinal glass. Consistent with this feature, the AMRO disappeared from Fig. 6(b), taken at 393 K, just after  $T_{\text{dev}}$ .

Figure 6(c) is taken at 403 K, just after  $T_c$ . Corresponding to the emergence of the crystalline structure, many circular lines with high intensity represent the Debye-Scherrer ring.

On the other hand, structural change corresponding to sub- $T_g$  endotherm was very tiny in the 2D diffraction pattern. For quantitative analysis, we calculate the 1D diffraction profile by taking the azimuthal average for the 2D diffraction pattern only over the direction of the AMRO structure. The average is taken over the region in the white triangle only shown in Fig. 7(a). Obtained 1D profiles are shown in Fig. 7(b). While the broad peak at around  $1.3 \text{ \AA}^{-1}$  colored with orange is the so-called halo peak which is typical in a glassy system, the peak around  $0.7 \text{ \AA}^{-1}$  colored with light blue corresponds to the AMRO structure. Like the observation in the 2D diffraction pattern, the intensity of the light blue region hardly changes in the temperature range of  $310 \sim 370 \text{ K}$ , where sub- $T_g$  endotherm occurs.

The insensitiveness of structural variance according to sub- $T_g$  endotherm is more clarified by the annealing experiment. Once the as-deposited sample is annealed at a temperature higher than 350 K, where sub- $T_g$  endotherm occurs, as is discussed in Sec.3.1, sub- $T_g$  endotherm completely disappears, then the accompanied structural change should be observed. Here, Fig. 8(a) represents the change in the 1D profile during the process of annealing for

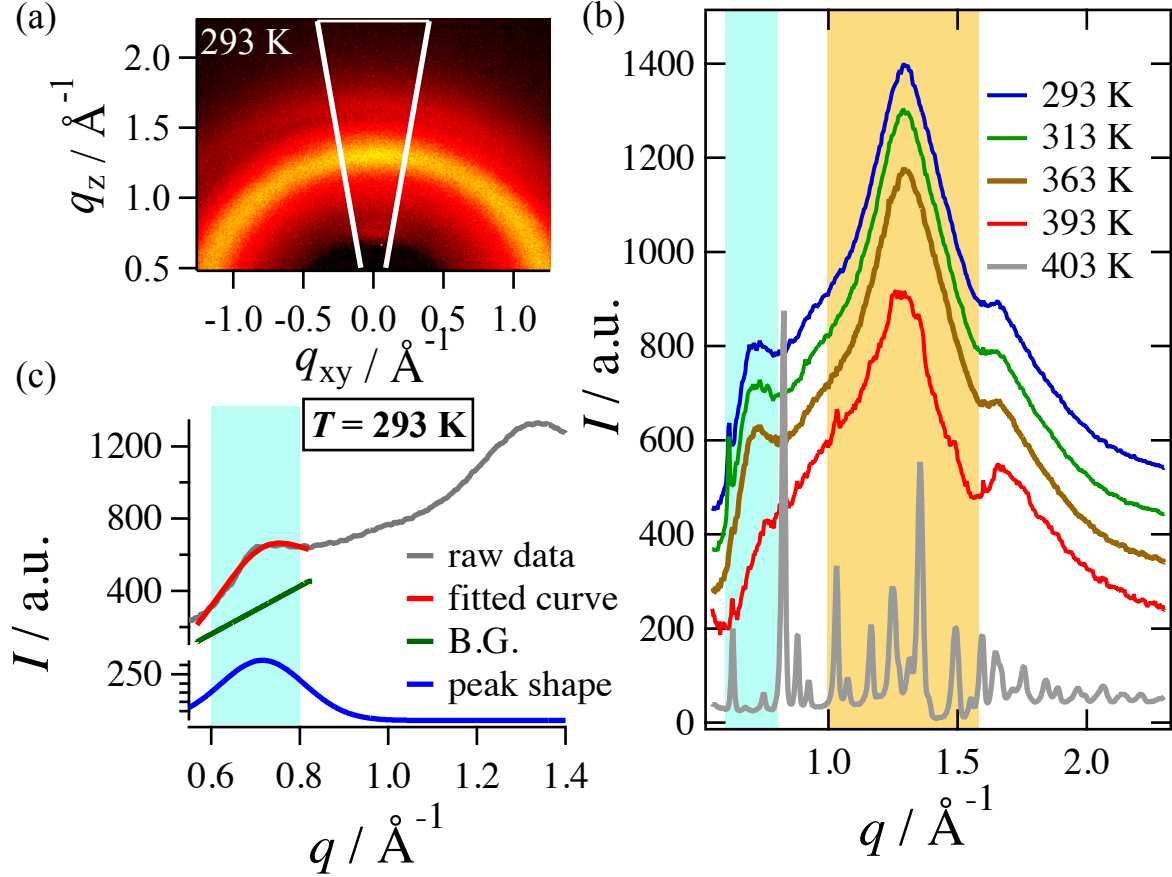


Figure 7: (a) indicates the schematics of the analysis of WAXD results by using the taken image for the as-deposited sample at 293 K. The white triangle indicates the region to elucidate the 1D profile. The center angle of the white fan shape is taken as small as possible while satisfying the condition that the region includes a broad bright spot and is about 30 degrees. (b) indicates the obtained 1D profile. Traces are shifted for readability. The trace for 403 K is multiplied by 0.1 to compare with other results. Light blue and yellow regions indicate MRO spots and halo peaks in Fig. (a). (c) indicates the summary of the analysis for the MRO spot.

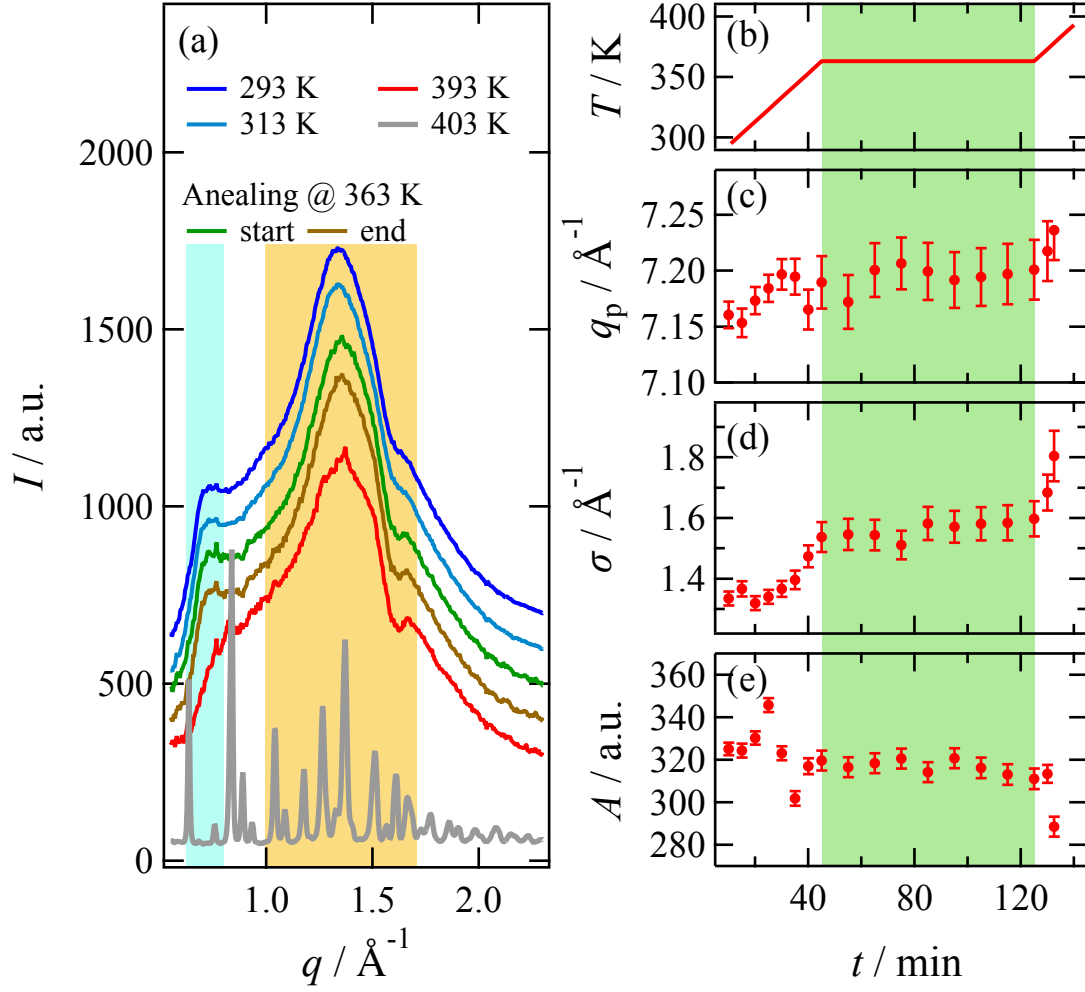


Figure 8: Time evolution of vapor-deposited glass with annealing sub- $T_g$  endotherm at 363 K. (a) indicates snapshots of 1D profile. Traces are shifted for readability. (b) indicates the temperature profile for this procedure. The peak position, peak width, and amplitude for the anomaly at the light blue region are shown in (c), (d), and (e), respectively.

the as-deposited sample at 363 K. To analyze quantitatively, the peak position ( $q_p$ ), the peak width ( $\sigma$ ), and the peak intensity ( $A$ ) are estimated by using a linear function for the background and a Gaussian function for the peak in the profile around  $0.7 \text{ \AA}^{-1}$  as follows:

$$I(q) = A \times \exp\left(-\frac{(q - q_p)^2}{\sigma^2}\right) + B.G. \quad (4)$$

Figures 8(b-e) represent temperature profile,  $q_p$ , the peak width ( $\sigma$ ), and the peak intensity ( $A$ ), respectively. While the annealing was performed in the  $45 \leq t/\text{min} \leq 125$ , none of the values changed much before and after the annealing. This means the AMRO structure could not be the origin of the sub- $T_g$  endotherm. In the one-dimensional profile shown here, no change associated with sub- $T_g$  endotherm was observed except near  $0.7 \text{ \AA}^{-1}$ , and it was found that it is difficult to understand sub- $T_g$  endotherm from the structural change in the region smaller than  $120 \text{ \AA}$  that WAXD can observe.

### 3.4. Comparison between high sensitive DSC and conventional DSC study

From here, we discuss the origin of sub- $T_g$  endotherm standing with the precise thermal measurements obtained by high-sensitive differential scanning calorimetry (HSDSC). Figure 9 represents excess heat capacities obtained by conventional DSC for ca.  $12 \text{ }\mu\text{m}$  and by HSDSC for the thickness of around  $250 \text{ nm}$ . Heat capacities for conventional DSC are identical to the results shown in Sec.3.1. For HSDSC measurements, results for three different deposition rates are shown. Following the notation expressed in Sec.3.2, the excess heat capacity is calculated as the difference between the glassy-liquid and crystalline states.

HSDSC results demonstrate the appearance of sub- $T_g$  endotherm, devitrification, and cold crystallization as same as conventional DSC results. At first, an apparent increase in the strength of sub- $T_g$  endotherm by HSDSC against conventional DSC should be pointed out. We will discuss that phenomenon in the following section. Next, the temperature shifts

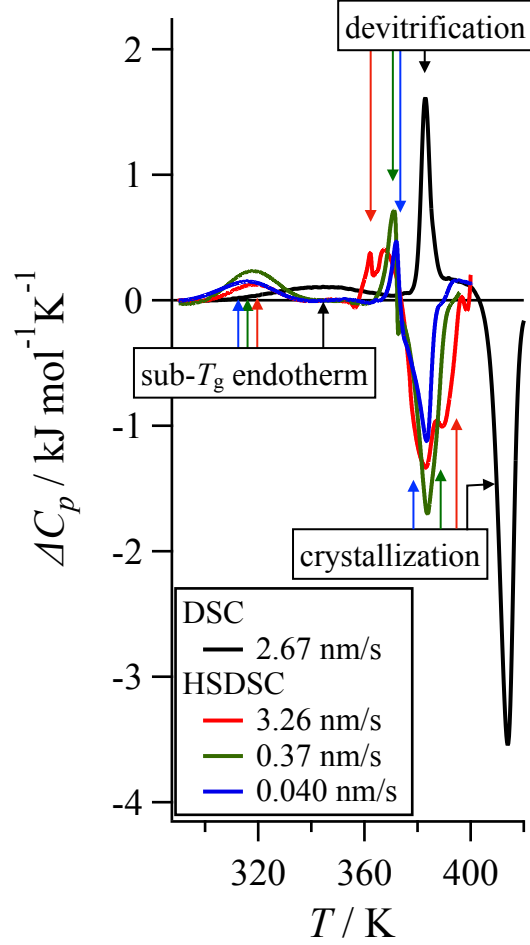


Figure 9: The overview of excess heat capacities obtained by DSC and HSDSC results. The black line indicates the result obtained by conventional DSC for  $v_d = 2.67$  nm/s with the thickness of  $11.8 \mu\text{m}$ . This trace is identical to the red line in Fig. 4(a). The red, green, and blue lines indicate  $\Delta C_p$ s for  $v_d$  of 3.26 nm/s, 0.37 nm/s, and 0.040 nm/s with the thickness of around 250 nm, respectively.

for the occurrences of sub- $T_g$  endotherm, devitrification, and cold crystallization in HSDSC against conventional DSC have drawn our attention. Consulting the difference in the scanning rate between HSDSC (1 K/min) and conventional DSC (10 K/min), those temperature shifts mean those anomalies should be a dynamic process rather than the transition between equilibrated states. Since the decrease on  $T_{\text{dev}}$  in HSDSC against conventional DSC is smaller than  $T_c$ , the competition emerges between devitrification and cold crystallization processes in HSDSC results.

### 3.5. Thickness dependencies of sub- $T_g$ endotherm

In this section, we discuss excess heat capacities obtained by HSDSC as a function of sample thickness,  $d$ , and deposition rate,  $v_d$  ranging from around 5 nm to 500 nm and 0.04 nm/s to 4.0 nm/s, respectively. Figures 10(a-c) show the excess heat capacities for different thicknesses with  $v_d$  in the same range. Deposition rates ( $v_d$ ) in Figs. 10(a-c) are approximately 0.05 nm/s, 0.5 nm/s, and 3.0 nm/s, respectively.

All figures show the strength of endothermic effects associated with sub- $T_g$  endotherm around 300-330 K increases as  $d$  decreases. On the other hand, the endothermic effects associated with the devitrification process are seen around 370 K and those strengths are also increasing with decreasing  $d$ . The degrees of increase against the variance of  $d$  are moderate compared to those in sub- $T_g$  endotherm.

Interestingly, the increase in the endothermic effect of sub- $T_g$  endotherm with a decrease in  $d$  was more significant for the lower deposition rates. The total amount of heat absorption associated with sub- $T_g$  endotherm,  $\Delta H_{\text{sub}}$ , was calculated as follows:

$$\Delta H_{\text{sub}} = \int_{T=T_{\text{min}}}^{T=T_{\text{max}}} \Delta C_p dT \quad (5)$$

Here,  $T_{\text{min}}$  and  $T_{\text{max}}$  are the lower and upper limits of the temperature at which sub- $T_g$  endotherm occurs. Figure 10(d) represents the log-log plot of  $d$  dependence of  $\Delta H_{\text{sub}}$ . The

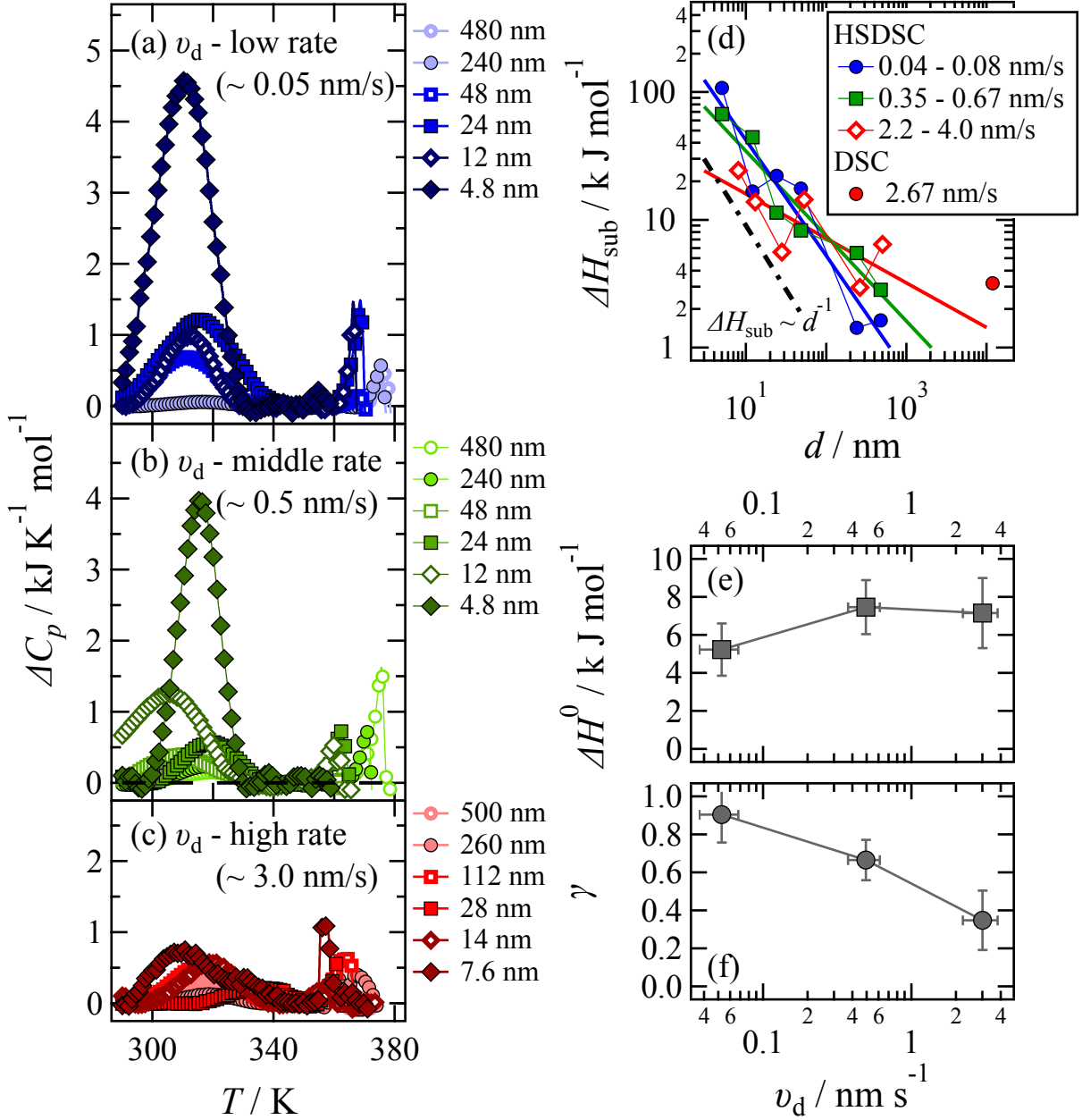


Figure 10: Summary of excess heat capacity,  $\Delta C_p$ , as a function of temperature concerning different thicknesses and deposition rates ( $v_d$ ). Figures (a-c) indicate thickness dependencies of  $\Delta C_p$  from small to high  $v_d$  as discussed in the main text, the strength of sub- $T_g$  endotherm becomes eminent with small  $d$ , in low  $v_d$  (d) denotes the total heat absorption associated with sub- $T_g$  endotherm as a function of inversed thickness. Results shown in Fig. (d) are fitted by Eq.(6) and fitted results are shown in Fig. (e) and (f), respectively.

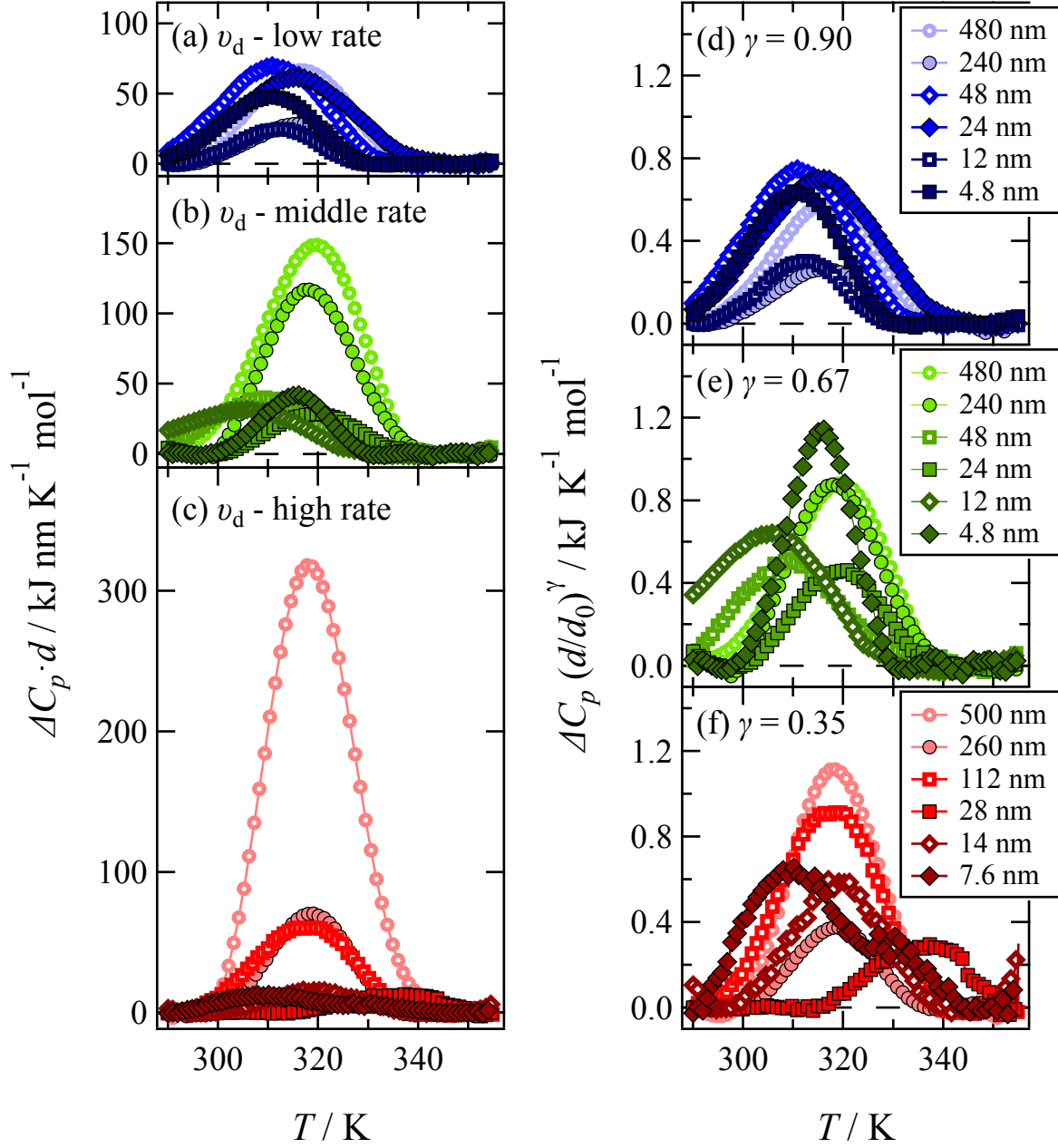


Figure 11: The schematics of scaling relation in  $\Delta C_p$  for sub- $T_g$  endotherm against thickness (left panel) and powers of thickness (right panel) are shown. The value of power in each  $v_d$  is taken from Fig. 10(f).

solid line in Fig.10(d) indicates the fitted line under the assumption of  $\Delta H_{\text{sub}}$  as a function of inversed power laws of  $d$  as,

$$\Delta H_{\text{sub}} = \Delta H^0 \times \left( \frac{d}{d_0} \right)^{-\gamma}. \quad (6)$$

Here,  $d_0$  is set to 100 nm. Along with the fitting results by Eq. (6), obtained values  $\Delta H^0$  and  $\gamma$  are displayed in Figs. 10(e,f), respectively. In the end, we found that 1)  $\Delta H_{\text{sub}}$  increases with the inversed power of sample thickness,  $d$ , 2) those exponents decrease with increasing the deposition rate,  $v_d$  and 3)  $\Delta H_{\text{sub}}$  has a constant value regardless of the deposition rate around  $d = 100$  nm. It is particularly noteworthy that the largest value of  $\Delta H_{\text{sub}} = 100$  kJ/mol was observed for the sample with a deposition rate of 0.08 nm/s and a thickness of 5 nm. This value exceeds the equilibrium melting enthalpy of phenolphthalein crystals,  $\Delta_{\text{fus}}H = 60$  kJ/mol, which means that the stability of ultrathin VD phenolphthalein glass surpassed the stability of its crystalline state.

### 3.6. Scaling for sub- $T_g$ endotherm and devitrification process by thickness

The total amount of heat absorption associated with sub- $T_g$  endotherm,  $\Delta H_{\text{sub}}$ , depends on the sample thickness,  $d$  as shown in Fig. 10. Those dependencies indicate the existence of scaling relation in sub- $T_g$  endotherm. Figure 11 summarizes the results of scaling relation for the heat capacity concerning  $d$ . While Figs. 11(a-c) represent the result of multiplying the heat capacity by  $d$ , Figs. 11(d-f) represent the normalization of the heat capacity based on the scaling relation (Eq. (6)).

The former corresponds to the case where  $\gamma = 1$ . If this scaling would work, sub- $T_g$  endotherm should be explained by the sample's total amount of surface area. This picture, the surface area scenario, has been previously introduced by Rodriguez et al. for the devitrification event in ultrastable vapor-deposited glass consideration with some kinds

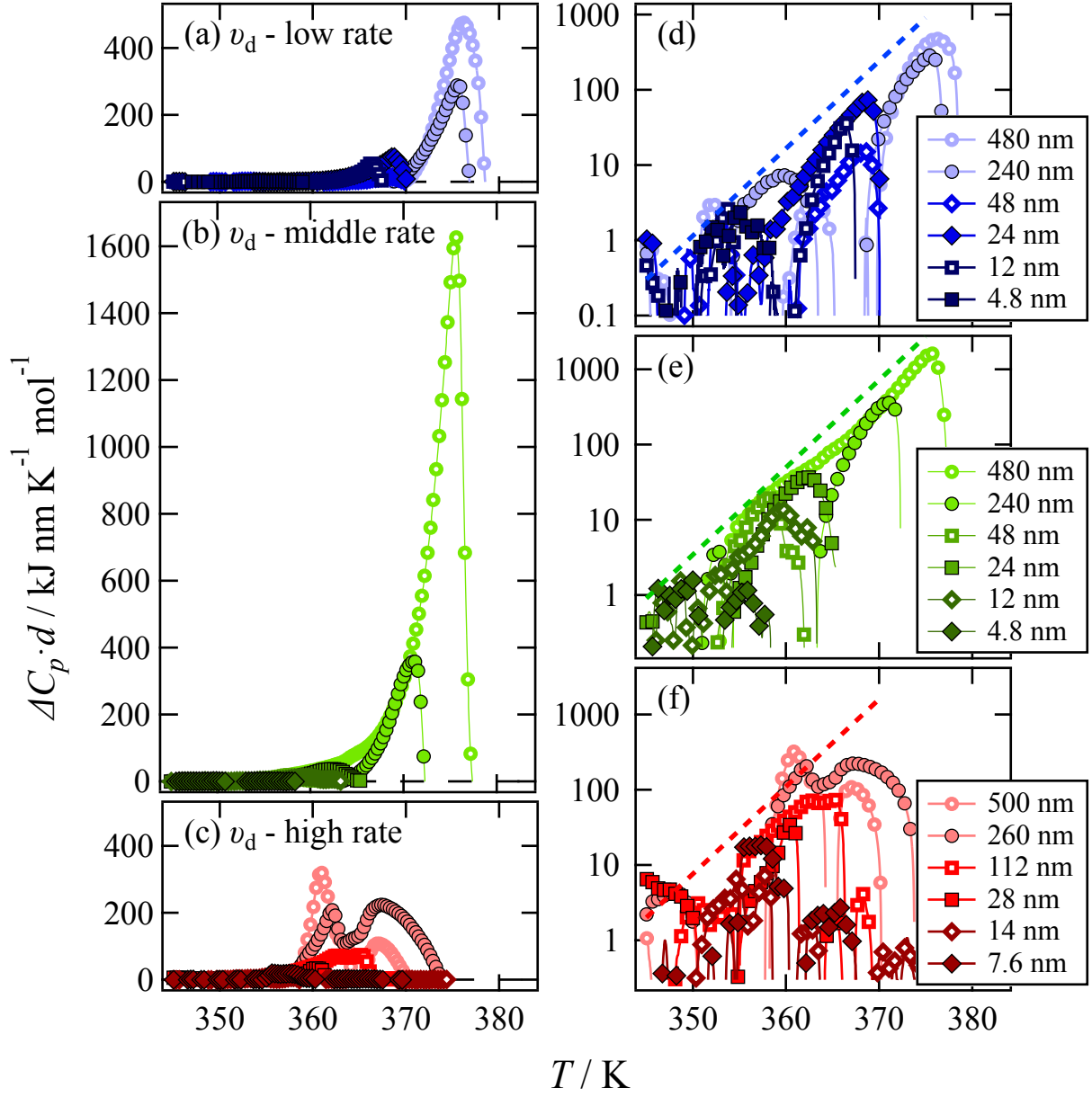


Figure 12: The schematics of scaling relation in  $\Delta C_p$  for devitrification process against thickness. The left and right panels indicate  $\Delta C_p$ s as a function of temperature as linear scale and log scale, respectively.

of transformation kinetics near the surface. The latter is, currently, the phenomenological description based on Eq. (6).

The surface area scenario would seem to work when the deposition rate,  $v_d$  is low. However, in case  $v_d$  would be high, while the surface area scenario would no longer be convincing, the phenomenological description shows a good scaling relation concerning  $d^\gamma$ . Then, understanding the phenomenological description is important for understanding sub- $T_g$  endotherm. On the other hand, the surface area scenario explains the devitrification event well, which is consistent with previous studies by Rodriguez *et al.*<sup>32,33</sup> Figure 12 summarizes the results of scaling of the heat capacity around the devitrification event. Figures 12(a-c) plot as linear scale and Figs. 12(e-f) represent the log scale. We think it is notable to comment that the dotted lines in Figs. 12(e-f) represent the identical functional form,  $\Delta C_p(T) \propto \exp(AT)$ , where  $A$  becomes  $0.267 \text{ K}^{-1}$ . It means the early stage of the devitrification follows the same temperature, *i.e.* time, dependence. We would not like to discuss further on that point since it is not the scope of this article.

## 4. Discussion - Schematics view of deposition process -

### 4.1. Microscopical description

Based on our results, we would like to propose a scenario to explain structure during the deposition process. The schematics of the whole process are shown in Fig. 13. We divide the process into two parts; pre-organization and reorganization.

Pre-organization is the independent *local* organization process during the deposition. The most comprehensive example is the first stage of the deposition. When the source molecules come to the clean deposited surface, molecules suffer no other interaction than the deposited “fixed” surface and are randomly stacked onto the surface with sustaining  $T_d$ . Since  $T_d$  is smaller than ordinal  $T_g$ , molecules are expected to be immobile. However, as Ruan *et al.*<sup>34</sup> showed the acceleration of surface mobility in VD glass, deposited molecules may have larger

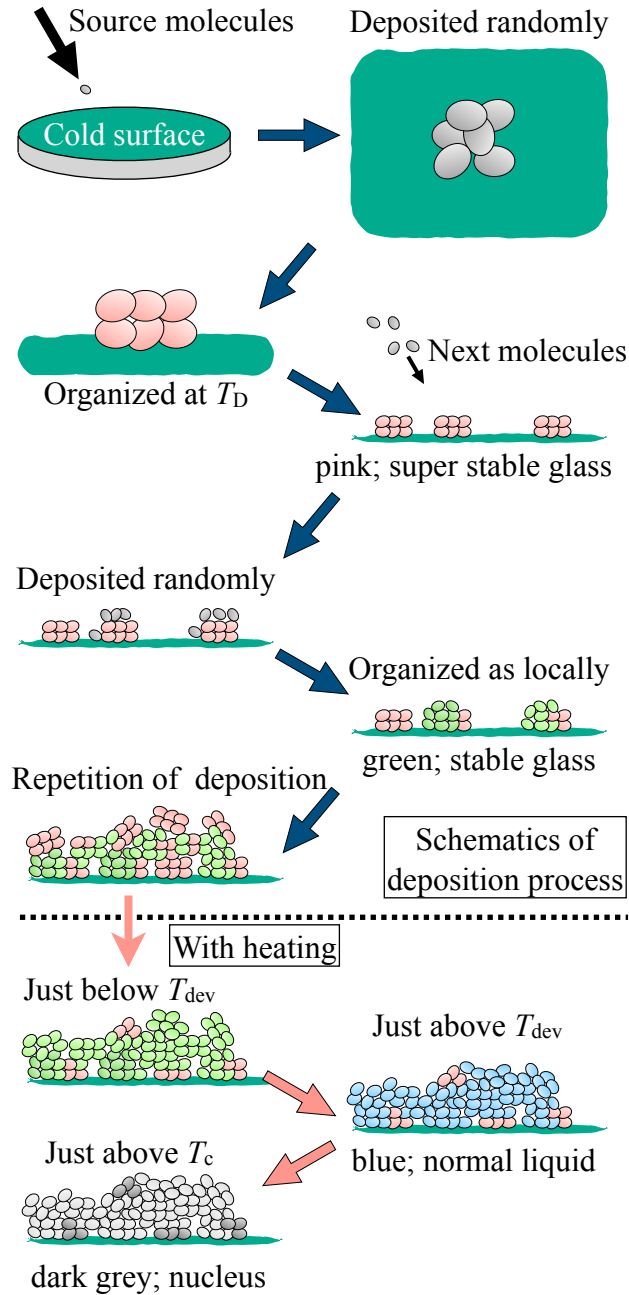


Figure 13: The schematics of the microscopical scenario for describing the feature of VD phenolphthalein glass. The top and the bottom panels indicate the deposition and heating processes, respectively. Pink, green, and blue molecules indicate super-stable, stable, and normal glass/liquid states, respectively. Upon heating, the super-stable glass turns into a nucleus (colored with dark).

mobility and organize the structure. At that time, in case the deposition rate is low, the number of molecules to organize should be small. Here, we think this smallness is the key to understanding the super stability. In general, the structure composed of a small number of molecules may locally have a lower entropic state than its crystalline state.<sup>35,36</sup> We think the origin of sub- $T_g$  endotherms is this super stable structure. Then we call this structure *super-stable glass* and is shown in Fig. 13 as pink.

Reorganization is the cooperative organization process during the deposition and temperature variation. During the deposition process, source molecules may stack onto the super-stable glass. Since the source molecules have large kinetic energy, once those are attached to the super-stable glass, the structure is locally energized and stabilized again. This process occurred with the neighboring molecules at the attached surface. Then the outcome of the resulting structure would have a middle-range order. We call this structure as a stable glass, sometimes called ultrastable glass. Those are shown in Fig. 13 as green.

Finally the devitrification temperatures of the super-stable (Temperature for sub- $T_g$  endotherm) and stable glass ( $T_{dev}$ ) play important role. Since the former is low and the latter is high, the source molecules do not energize the stable glass and turn to be super-stable glass and do energize the super-stable glass and turn to be stable glass, respectively.

Following that scenario, sub- $T_g$  endotherm occurred during the heating process would be explained as a transformation process from super-stable glass (pink) to stable glass (green) as shown in the bottom panel of Fig. 13. Moreover, owing to the high stability in super-stable glass, the remaining part of super-stable glass after sub- $T_g$  endotherm event would play a role for the nucleus. This is supported by experimental insight, that vapor-deposited phenolphthalein is very easy to crystallize after devitrification.

#### 4.1. Macroscopical description

Macroscopically, that idea would be interpreted as a free-energy scenario. We are not the first people to come up with the idea of a highly stabilized structure in a small amount of

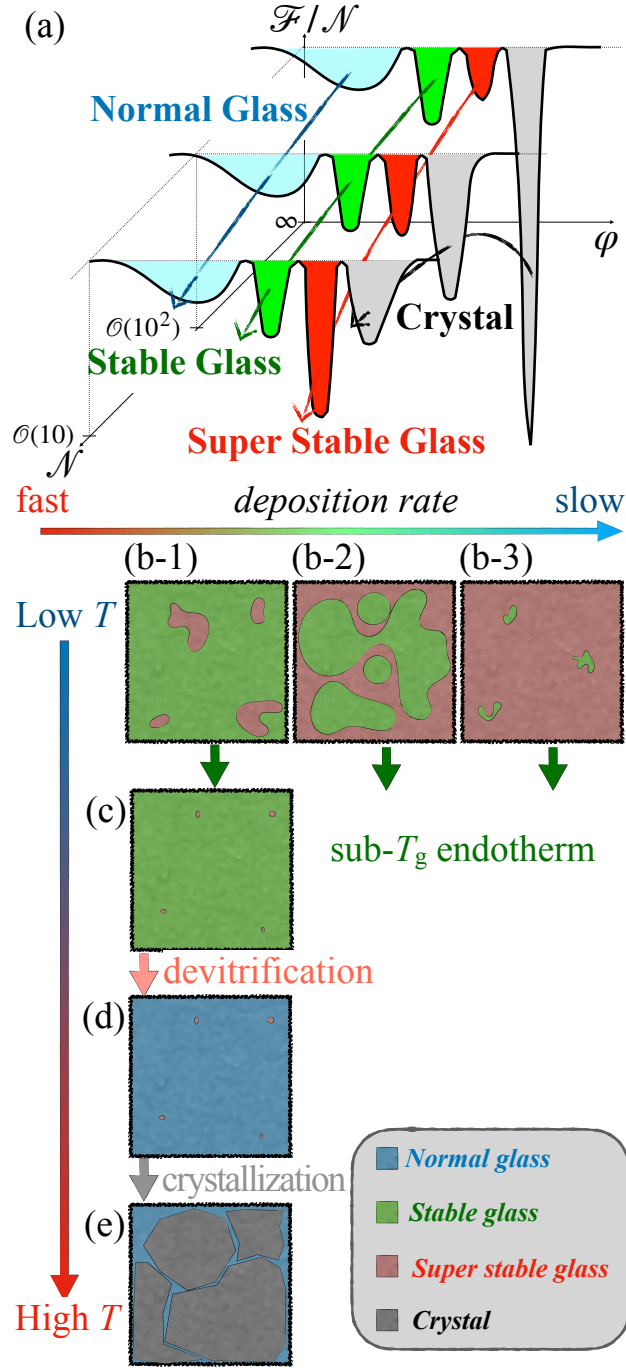


Figure 14: The schematics of the macroscopical scenario for describing the deposition process. Figure (a) indicates the free energy landscape as a function of the number of constituent molecules. Figure (b) indicates the deposited surface just after the deposition process. The slower the deposition rate, the region of super stable glass is increasing. With taking Fig. (b) as an initial condition, the system evolves with heating according to Figs. (c-e).

molecules. As discussed in Sec.4.1., in the old days, Sir. Frank demonstrates a locally stabilized structure as a tetrahedron that could not make long-range order.<sup>35</sup> More recently, Josh et al. proposed a scenario to describe local free energy with a finite amount of molecules.<sup>36</sup> In this work, they confirmed bimodal free energy distribution in a hard sphere system for 12 molecules. It means the existence of a locally stabilized structure more stable than a normal crystalline state at a small number of molecules. On that basis, we propose the model selection of the favored structure dependent on the number of constituent molecules.

The schematics of this idea are shown in Fig.14. Figure 14(a) represents a free energy landscape according to the number of constituent molecules in a system. From back to front, the number of constituent molecules is  $\infty$ ,  $\mathcal{O}(10^2)$ , and  $\mathcal{O}(10)$ , respectively. Following the discussion made before, we assume the existence of three branches in the free energy landscape as a glassy state. The local minimum illustrated in blue represents the branch for ordinal glass and over-quenched liquid. This is equivalent to a conventional free energy landscape scenario. At most, the typical number of molecules in the glassy structure is around  $\mathcal{O}(10)$ . This means the depth of the free energy landscape for this minimum does not vary with the number of molecules. The local minimum illustrated in green represents the branch for stable glass. We still do not have any evidence of the number of molecules contributing to a stable structure. Although the situation was not to be said to achieve stable glass, calculations for vapor-deposited glass based on heat capacity measurement were previously done by ST, and the largest one was found to be approximately 7 in propene.<sup>17</sup> Then, the number of molecules associated with stable glass is assumed to be almost the same for conventional glass. Then, the depth of free energy landscape for this branch is almost the same concerning the number of molecules. Next, the local minimum illustrated in pink represents the branch for super-stable glass. We think this structure is essentially the same as the structure that Frank or Josh et al previously inferred. This structure should be stabilized only for a tiny amount of molecules and not in the system where the number of molecules is larger than  $\mathcal{O}(10^2)$ . Reflecting this consideration, this branch's free energy

landscape depth is drawn as the deepest in  $\mathcal{O}(10)$ . At last, the number of molecules for the crystalline state, which is drawn as a grey branch, should be considered. As we find the size dependences of melting temperature in many crystalline structures, this branch's depth of free energy landscape is shallower in smaller amounts of molecules. Based on the above discussion, the preparation and the evolution of the deposited surface is illustrated as Figs. 14(b-e).

## 5. Conclusion

The key findings of this study are 1) the discovery of sub- $T_g$  endotherm at below ordinal  $T_g$ , 2-a) sub- $T_g$  endotherm is scaled with the power of inversed thickness, and 2-b) those powers become about unity at a low deposition rate while go to 0 by increasing deposition rate, 3) the stability estimated by the total amount of heat absorption becomes as much as the crystalline state at around that thickness of 100 nm, and 4) there is no significant structure such as long-ranged order in the crystalline state nor middle ranged structure in ultrastable vapor-deposited glass associated with sub- $T_g$  endotherm.

With the standpoints from the study on the glassy systems, not much but definitely, some reports on the phenomenon relevant with sub- $T_g$  endotherm are found in several systems such as metallic glass,<sup>26</sup> inorganic glass,<sup>37</sup> etc. In most cases, sub- $T_g$  endotherm emerges from the annealing of the lengthy time at lower than ordinal  $T_g$ . The discussion on the relation between sub- $T_g$  endotherm and known mechanisms such as  $\beta$  relaxation as represented by the Johari-Goldstein mode,<sup>26</sup> modified Tool-Moynihan-Narayanaswamy model, creation of nanocrystals, etc, has been made but is not clear. Considering the relevancy with the outcome of our results, the effect of the enhancement of activities on the surface is also plausible to consider for those systems.

## Acknowledgement

The synchrotron X-ray scattering experiments were performed in a BL40B2 at the SPring-8 with the approval of the SPring-8 Proposal Review Committee (BL40B2: 2017B1390/2018A1487/ 2018B1525/ 2019A1472).

## References

- (1) Berthier, L.; Ediger, M. D. Facets of glass physics. *Phys. Today* **2016**, *69*, 40.
- (2) Watanabe, T.; Shiozawa, M.; Tatsu, E.; Kimura, S.; Umeda, M.; Mine, T.; Shimotsuma, Y.; Sakakura, M.; Nakabayashi, M.; Miura, K. *et al.* A driveless read system for permanently recorded data in fused silica. *Jpn. J. Appl. Phys.* **2013**, *52*, 09LA02.
- (3) Anderson, P.; Black, R.; Čerkauskaitė, A.; Chatzieleftheriou, A.; Clegg, J.; Dainty, C.; Diaconu, R.; Donnelly, A.; Drevinskas, R.; Gaunt, A. L. *et al.* Glass: A new media for a new era? 10th USENIX Work. Hot Top. Storage File Syst. HotStorage 2018, co-located with USENIX ATC 2018. Boston, MA, 2018.
- (4) Kawakami, K. Modification of physicochemical characteristics of active pharmaceutical ingredients and application of supersaturatable dosage forms for improving bioavailability of poorly absorbed drugs. *Adv. Drug Deliv. Rev.* **2012**, *64*, 480–495.
- (5) Jermain, S. V.; Brough, C.; Williams, R. O. Amorphous solid dispersions and nanocrystal technologies for poorly water-soluble drug delivery – An update. *Int. J. Pharm.* **2018**, *535*, 379–392.
- (6) Sakurai, M.; Furuki, T.; Akao, K. I.; Tanaka, D.; Nakahara, Y.; Kikawada, T.; Watanabe, M.; Okuda, T. Vitrification is essential for anhydrobiosis in an African chironomid, *Polypedilum vanderplanki*. *Proc. Natl. Acad. Sci. U. S. A.* **2008**, *105*, 5093–5098.

- (7) Weng, L.; Ziaei, S.; Elliott, G. D. Effects of Water on Structure and Dynamics of Trehalose Glasses at Low Water Contents and its Relationship to Preservation Outcomes. *Sci. Rep.* **2016**, *6*, 1–10.
- (8) Oka, R.; Yato, T.; Yamakawa, K.; Yao, H.; Tatsumi, S. Discovery of new thermal anomalies in trehalose dihydrate: insights into their properties through differential scanning calorimetry and microscopic observation. *J. Therm. Anal. Calorim.* **2024**,
- (9) BOUCHAUD, J.-P.; CUGLIANDOLO, L. F.; KURCHAN, J.; MÉZARD, M. *Spin Glas. Random Fields*; 1997; pp 161–223.
- (10) Bellon, L.; Ciliberto, S.; Laroche, C. Memory in the aging of a polymer glass. *Europhys. Lett.* **2000**, *51*, 551–556.
- (11) Bouchaud, J.-P. Aging in glassy systems: New experiments, simple models, and open questions. *Soft Fragile Matter* **2004**, 0–25.
- (12) Zhao, J.; Simon, S. L.; McKenna, G. B. Using 20-million-year-old amber to test the super-Arrhenius behaviour of glass-forming systems. *Nat. Commun.* **2013**, *4*, 1783.
- (13) Pérez-Castañeda, T.; Jiménez-Riobóo, R. J.; Ramos, M. A. Two-Level Systems and Boson Peak Remain Stable in 110-Million-Year-Old Amber Glass. *Phys. Rev. Lett.* **2014**, *112*, 165901.
- (14) Ediger, M. D. Perspective: Highly stable vapor-deposited glasses. *J. Chem. Phys.* **2017**, *147*, 210901.
- (15) Royall, C. P.; Turci, F.; Tatsumi, S.; Russo, J.; Robinson, J. The race to the bottom: approaching the ideal glass? *J. Phys. Condens. Matter* **2018**, *30*, 363001.
- (16) Takeda, K.; Yamamuro, O.; Oguni, M.; Suga, H. Thermodynamic characterization of vapor-deposited amorphous solid. *Thermochim. Acta* **1995**, *253*, 201–211.

- (17) Tatsumi, S.; Aso, S.; Yamamuro, O. Thermodynamic study of simple molecular glasses: Universal features in their heat capacity and the size of the cooperatively rearranging regions. *Phys. Rev. Lett.* **2012**, *109*, 045701.
- (18) Kearns, K. L.; Swallen, S. F.; Ediger, M. D.; Wu, T.; Sun, Y.; Yu, L. Hiking down the Energy Landscape: Progress Toward the Kauzmann Temperature via Vapor Deposition. *J. Phys. Chem. B* **2008**, *112*, 4934–4942.
- (19) Ramos, S. L. L. d. M. Thermal characterization of molecular glasses vapor-deposited at diverse temperatures and interpretation of the characters in terms of anisotropic intermolecular interaction. Ph.D. thesis, Tokyo Institute of Technology, 2011.
- (20) L. M. Ramos, S. L.; Chigira, A. K.; Oguni, M. Devitrification Properties of Vapor-Deposited Ethylcyclohexane Glasses and Interpretation of the Molecular Mechanism for Formation of Vapor-Deposited Glasses. *J. Phys. Chem. B* **2015**, *119*, 4076–4083.
- (21) Pérez-Castañeda, T.; Rodríguez-Tinoco, C.; Rodríguez-Viejo, J.; Ramos, M. A. Suppression of tunneling two-level systems in ultrastable glasses of indomethacin. *Proc. Natl. Acad. Sci. U. S. A.* **2014**, *111*, 11275–11280.
- (22) Dawson, K. J.; Zhu, L.; Yu, L.; Ediger, M. D. Anisotropic structure and transformation kinetics of vapor-deposited indomethacin glasses. *J. Phys. Chem. B* **2011**, *115*, 455–463.
- (23) Lyubimov, I.; Antony, L.; Walters, D. M.; Rodney, D.; Ediger, M. D.; De Pablo, J. J. Orientational anisotropy in simulated vapor-deposited molecular glasses. *J. Chem. Phys.* **2015**, *143*.
- (24) Bishop, C.; Thelen, J. L.; Gann, E.; Toney, M. F.; Yu, L.; DeLongchamp, D. M.; Ediger, M. D. Vapor deposition of a nonmesogen prepares highly structured organic glasses. *Proc. Natl. Acad. Sci.* **2019**, *116*, 21421–21426.

- (25) Chua, Y. Z.; Tylinski, M.; Tatsumi, S.; Ediger, M. D.; Schick, C. Glass transition and stable glass formation of tetrachloromethane. *J. Chem. Phys.* **2016**, *144*, 244503.
- (26) Yu, H.-B. H.-B.; Luo, Y.; Samwer, K. Ultrastable Metallic Glass. *Adv. Mater.* **2013**, *25*, 5904–5908.
- (27) Yu, H. B.; Wang, W. H.; Bai, H. Y.; Samwer, K. The  $\beta$ -relaxation in metallic glasses. *Natl. Sci. Rev.* **2014**, *1*, 429–461.
- (28) Yu, H. B.; Tylinski, M.; Guiseppi-Elie, A.; Ediger, M. D.; Richert, R. Suppression of  $\beta$  Relaxation in Vapor-Deposited Ultrastable Glasses. *Phys. Rev. Lett.* **2015**, *115*, 1–5.
- (29) Kishimoto, D.; Hanabusa, A.; Saruyama, Y.; Yao, H. unpublished.
- (30) Wang, S.; Tozaki, K.; Hayashi, H.; Inaba, H. Nano-watt stabilized DSC and its applications. *J. Therm. Anal. Calorim.* **2005**, *79*, 605–613.
- (31) Sepúlveda, A.; Leon-Gutierrez, E.; Gonzalez-Silveira, M.; Rodríguez-Tinoco, C.; Clavaguera-Mora, M. T.; Rodríguez-Viejo, J. Accelerated Aging in Ultrathin Films of a Molecular Glass Former. *Phys. Rev. Lett.* **2011**, *107*, 025901.
- (32) Rodríguez-Tinoco, C.; Gonzalez-Silveira, M.; Ràfols-Ribé, J.; Lopeandía, A. F.; Clavaguera-Mora, M. T.; Rodríguez-Viejo, J. Evaluation of growth front velocity in ultrastable glasses of indomethacin over a wide temperature interval. *J. Phys. Chem. B* **2014**, *118*, 10795–10801.
- (33) Rodríguez-Tinoco, C.; Gonzalez-Silveira, M.; Ràfols-Ribé, J.; Lopeandía, A. F.; Rodríguez-Viejo, J. Transformation kinetics of vapor-deposited thin film organic glasses: The role of stability and molecular packing anisotropy. *Phys. Chem. Chem. Phys.* **2015**, *17*, 31195–31201.
- (34) Ruan, S.; Zhang, W.; Sun, Y.; Ediger, M. D.; Yu, L. Surface diffusion and surface crystal growth of tris -naphthyl benzene glasses. *J. Chem. Phys.* **2016**, *145*.

- (35) Frank, F. C. Supercooling of Liquids. *Proc. R. Soc. A Math. Phys. Eng. Sci.* **1952**, *215*, 43–46.
- (36) Robinson, J. F.; Turci, F.; Roth, R.; Royall, C. P. Morphometric approach to many-body correlations in hard spheres. *Phys. Rev. Lett.* **2019**, *122*, 68004.
- (37) Yue, Y.; Angell, C. A. Clarifying the glass-transition behaviour of water by comparison with hyperquenched inorganic glasses. *Nature* **2004**, *427*, 717–20.